EFFECT OF CeO$_2$ DOPING ON THE MICROSTRUCTURE AND CORROSION BEHAVIOR OF CoCuNiTi HIGH-ENTROPY ALLOY COATINGS

VPLIV DOPIRANJA CeO2 NA MIKROSTRUKTURO IN KOROZIJO VISOKO-ENTROPIJSKIH PREVLEK IZ ZLITIN NA OSNOVI CoCuNiTi

Ming-xing Ma, Liang Zhao, Zhi-xin Wang[*], Shang-zhi Li, Chen Dong

School of Materials and Chemical Engineering, Zhongyuan University of Technology, 41 Zhongyuan Road, Zhengzhou 450007, P. R. China

CoCuNiTi high-entropy alloy coatings with an equal molar ratio were prepared on 45 steel substrates using the laser-cladding method. The effect of CeO$_2$ doping on phase structure, microstructure and corrosion behavior of CoCuNiTi coatings were investigated by X-ray diffraction, optical microscope, scanning electron microscope, and electrochemical workstation. The results show that the phase structure of CoCuNiTi coating doped with 1 *w*/% CeO$_2$ is transformed from the original dual-phase structure of FCC main phase and BCC phase to the dual-phase structure of BCC main phase and FCC phase, mainly because CeO$_2$ addition helps to improve the temperature gradient and solidification rate during solidification, reduce the nucleation resistance and the diffusion distance of the alloying elements, and provide a liquid environment with longer time, lower viscosity and higher diffusion rate. The microstructure of the two coatings is composed of BCC-phase dendrite and FCC-phase interdendrite. The widths of the primary dendrites of the columnar dendrites in CoCuNiTi cladding layer before and after CeO$_2$ doping are about 8.10 μm and 6.51 μm, respectively. The CoCuNiTi coating doped with 1 *w*/% CeO$_2$ has the smallest corrosion current density, the largest capacitive reactance arc radius and polarization resistance, and the best corrosion resistance in 3.5 *w*/% NaCl solution, which is mainly due to making the alloy structure refined and the element distribution uniform after the CeO$_2$ addition.

Keywords: high-entropy alloy coating, CoCuNiTi, microstructure, corrosion behavior, laser cladding

Avtorji v pričujočem članku opisujejo pripravo s CeO$_2$ dopiranih prevlek na osnovi visoko-entropijskih zlitin tipa CoCuNiTi z enakim molarnim razmerjem. Prevleke so nanašali na jekleno podlago (konstrukcijsko jeklo 0,45–0,5 *w*/% C) z laserskim postopkom. Nato so študirali vpliv dopiranja s CeO$_2$ na fazno sestavo, mikrostrukturo in korozijo CoCuNiTi prevlek z rentgensko difrakcijo, z opazovanjem pod svetlobnim (LM) in vrstičnim elektronskim mikroskopom (SEM) in na elektro-kemijski celici. Rezultati raziskav in opazovanj so pokazali, da dodatek 1 *w*/% CeO$_2$ spremeni dvofazno, pretežno ploskovno in delno prostorsko centrirano kubično (FCC-BCC) mikrostrukturo CoCuNiTi prevlek v pretežno prostorsko in delno ploskovno centrirano kubično mikrostrukturo, kar izboljša temperaturni gradient in hitrost strjevanja med ohlajanjem oz. strjevanjem zlitine, zmanjša upor proti nukleaciji, zmanjša difuzijsko razdaljo med legirnimi elementi ter zagotavlja daljši čas prisotnosti taline, manjšo viskoznost in večjo hitrost difuzije. Mikrostruktura dveh prevlek je bila sestavljena iz dendritne BCC in med-dendritne FCC faze. Širini primarnih dendritov CoCuNiTi prevlek pred in po dopiranju s CeO$_2$ sta bili 8,10 μm oziroma 6,51 μm. Prevleka CoCuNiTi dopirana z 1 *w*/% CeO$_2$ je imela manjšo korozijsko tokovno gostoto, večjo kapacitivno upornost polmera obloka in polarizacijsko upornost ter najboljšo korozijsko odpornost v 3,5 *w*/% NaCl raztopini v glavnem zaradi izboljšane mikrostrukture zlitine in enakomerne porazdelitve elementov po dodatku CeO$_2$.

Keywords: prevleke na osnovi visoko-entropijskih zlitin, CoCuNiTi, mikrostruktura, korozija, lasersko nanašanje prevlek

1 INTRODUCTION

The high-entropy alloy (HEA) is considered to be a new direction for the development of the next generation of metal materials because of the variety of main alloying elements, the formation of simple solid-solution phase structure, and a series of excellent properties such as high hardness, high wear resistance, good corrosion and oxidation resistance.[1–8] With the continuous development and improvement of the research field and theoretical system of high entropy alloys, the number of main elements in this alloy has expanded from no less than 5 to more than 4; the alloy phase structure has also extended from single-phase face-centered cubic (FCC) or body-centered cubic (BCC) to a single-phase or multi-phase structure. HEA applications have also been expanded, such as tool coatings, drill bits, high-wear-resistant gears.

Laser cladding is a common coating processing technology, which uses a high-energy density laser beam to irradiate the cladding material to quickly melt it together with the metal substrate, and then rapidly cool and solidify to form a coating with specific properties. Laser cladding high-entropy alloy coating (HEAC) usually enhances its solubility with the substrate due to its variety of elements. It can form a transition layer with strong bonding force and excellent performance, and has become a common surface-strengthening method.[3–10] Wan et al.[7] prepared an Al$_{0.4}$CoCu$_{0.6}$NiSi$_{0.2}$Ti$_{0.25}$ HEAC with a dual-phase structure of FCC and BCC, and a good metal-

*Corresponding author's e-mail:
zxwang72@163.com (Zhi-xin Wang)

lurgical bond was formed between the coating and the substrate. Due to the increase in dislocation density and the number of grain boundaries, this coating has higher hardness and better corrosion resistance than the substrate, but there are obvious cracks in the coating. Zhang et al.[8] prepared CoCrFeNiTi HEAC with a FCC main phase, Fe- and Cr-rich simple cubic (SC) phase and $CoTi_2$-type Laves phase structure. The microstructure was composed of the bonding zone and the cladding zone. In the bonding region between the coating and the substrate, there is an obvious metallurgical bonding area and a typical columnar dendrite (DR) with the growth direction perpendicular to the interface. Peng et al.[9] prepared an $Al_2CrFeCoCuTiNi_x$ HEAC with FCC and BCC structures. The cladding zone is mainly composed of an axial crystal, nano crystal and white fine crystal, and there are a few holes in the cladding zone. In 3.5 w/% NaCl solution, the HEAC corrosion resistance first increases and then decreases with an increase in the Ni content, indicating that it has a good protective effect on the substrate. Qiu et al.[10] prepared an $Al_2CrFeCo_xCuNiTi$ HEAC on a Q235 substrate. The cladding zone is mainly composed of equiaxed crystal grains, as well as "cat-foot-shaped" grains and "snowflake" grains distributed in the matrix grains. This laser cladding coating has crack defects due to thermal stress. However, the defects such as cracks and holes are easy to appear in the laser cladding coating because of the short residence time at high temperature and the fast-cooling rate, which will adversely affect the mechanical properties and corrosion resistance of the coating.[7–11] The addition of rare-earth (RE) elements or their oxides can refine the alloy microstructure, purify the molten alloy and improve the casting performance, which is helpful for reducing the defects during solidification of the liquid metal.[12–16] For example, CeO_2 can decompose and release Ce atoms.[14] As a surface-active element, Ce can significantly reduce the surface energy and nucleation resistance, refine the HEA structure and reduce the defects.[12,13] At present, there are few reports on the preparation of CoCuNiTi HEAC on 45 steels by laser cladding, and there are no reports of the influence of rare-earth oxides on the microstructure and electrochemical property of this alloy. Therefore, in view of these points, CoCuNiTi HEAC was prepared on the surface of 45 steel by laser cladding in this study, and the effects of CeO_2 doping on the phase structure, microstructure and corrosion behavior of the alloy coating were investigated in detail. This will provide theoretical guidance for the improvement of theoretical system and subsequent research for CoCuNiTi HEAC.

2 EXPERIMENTAL PART

The CoCuNiTi HEAC was fabricated by the laser-cladding method. The pure metals of Co, Cu, Ni and Ti with a particle size of 200 mesh and a purity higher than 99.5 w/% (mass fraction) were used as raw materials. The CoCuNiTi alloy powder was weighed according to the equal atomic ratio, and was ground in a mortar for 30 min. The 45 steel substrate was polished and cleaned with sandpaper and anhydrous ethanol, respectively, then the ground metal powder and binder were mixed and prefabricated on the 45 steel substrate surface, and the above prefabricated sample was dried in a DHG-9123A constant-temperature drying oven. Finally, the laser cladding was carried out by using FL-DLight3-4000 high-power semiconductor laser and ABB IRB4500 six-axis industrial robot system. The laser power was 3 kW, the scanning speed was 5 mm/s, and the spot diameter was 6 mm. High-purity argon was used as the protection gas in the laser-cladding process, the gas pressure was 1.1 GPa, and the gas flow rate was 15 L/min. The raw materials of CoCuNiTi doped with CeO_2 were the above-mentioned pure metals and CeO_2 powder with a purity higher than 99.9 w/% and a particle size of 200 mesh. The doping ratio of the CeO_2 was 1 w/%, and the preparation process was exactly the same as that of the undoped sample.

The cladding samples were cut into 10 mm × 10 mm × 5 mm block samples by DK-M140 wire-cut electric discharge machine. The phase analysis was identified by X-ray diffraction (XRD) analysis using a Rigaku Ultima IV X-ray diffractometer with $Cu \cdot K_\alpha$ radiation operated at 40 kV and 200 mA in the range of 2θ from 30° to 90°. Metallographic photos were taken by a ZEISS DMM-150C optical microscope (OM). The morphology of the samples was observed in a PHENOM PROX scanning electron microscope (SEM). The electrochemical impedance and the potentiodynamic polarization curve of the samples were measured by the CHI760E electrochemical workstation. The three-electrode system was used in the experiment, the sample to be tested was used as the working electrode (WE), the reference electrode was used as the saturated calomel electrode (SCE), and the platinum plate electrode was used as the counter electrode (CE). The electrolyte was 3.5 w/% NaCl solution. A volume of 500 mL was selected each time, and the electrochemical test was started after immersion in the electrolyte for 20 min. The starting voltage of the potentiodynamic polarization curve was set to –1.5 V, the termination voltage was set to 0.5 V, and the scanning speed is 2 mV/s. The frequency of the impedance test was 0.01–100000 Hz, and the amplitude was 5 mV. All the above tests were completed at room temperature.

3 RESULTS AND DISCUSSION

Figure 1 is the X-ray diffraction patterns of the CoCuNiTi HEAC without and with 1 w/% CeO_2. The space group, lattice constant, cell volume, density and relative content of the two phases were obtained by whole pattern fitting and Rietveld refinement (see **Table 1**). The refinement weight factors (R) of the X-ray diffraction data for the CoCuNiTi coating without and
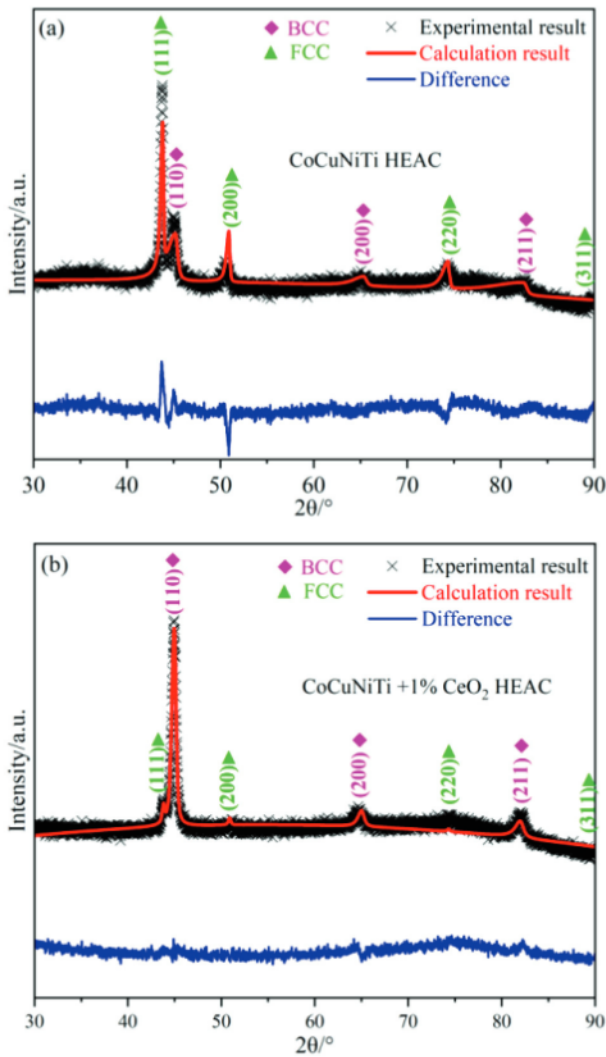
Figure 1: Experimental calculation and difference values of X-ray diffraction of HEACs: a) CoCuNiTi, b) CoCuNiTi + 1 *w*/% CeO₂

with CeO₂ were 6.82 *w*/% and 4.02 *w*/%, respectively. It can be seen from **Figure 1** that the phase structures of the two coatings are dual-phase structures composed of FCC and BCC. The diffraction peaks of FCC and BCC are (111), (200), (220), (311) and (110), (200), (211), respectively. From **Figure 1** and **Table 1**, the dual-phase structure changed from the original FCC main phase (66.9 *w*/%) and BCC phase (33.1 *w*/%) to BCC main phase (95.7 *w*/%) and FCC phase (4.3 *w*/%) after adding CeO₂. For CoCuNiTi HEAC, the reasons for the relatively high content of FCC phase are:

1) Ti with the highest melting point (see **Table 2**) can preferentially meet the supercooling requirements for nucleation and growth during the melt cooling process, but Ti having BCC structure (a stable BCC structure β-Ti above 882.5 °C) in the alloy melt are surrounded by a large number of atoms of other alloying elements with the FCC structure (Co is FCC structure above 417 °C) due to the maximum negative mixing enthalpy between Ti and other alloying elements (see **Table 3**) and no negative mixing enthalpy between other alloying elements except for Ti, which makes the diffusion distance and resistance of the alloying elements increase in the further growth of the precipitated Ti-rich particle. The mixing-enthalpy data in **Table 3** are from literature reports,[17,18] and the atomic radius difference δ can be calculated using the following equation[19]:

$$\delta = \sqrt{\sum_{i=1}^{N} c_i \left(1 - \frac{r_i}{\bar{r}}\right)^2} \qquad (1)$$

$$\bar{r} = \sum_{i=1}^{N} c_i r_i \qquad (2)$$

where N is the number of components, c_i is the mole percentage of component i and $\sum_{i=1}^{N} c_i = 1$, and r_i is the atomic radius of component i, Δr is the average atomic radius of each component in the alloy.

2) Because the laser-cladding process has a faster cooling rate and the precipitation and growth of Ti are limited by the above factors, other alloying elements with the FCC structure attach to the surface of the first precipitated Ti-rich particles and form a lot of heterogeneous nucleation, which further blocks the growth of the Ti-rich BCC phase.

3) After the pure metal raw materials are melted, the atomic clusters in the melt have the characteristics of short-range order and long-range disorder, that is to say, the atomic arrangement of the first coordination sphere of the atomic cluster in the melt is closer to that of the close-packed plane in the solid. In the rapid-cooling process, the diffusion resistance and viscosity of the alloy melt will increase rapidly, and it is easy to form the FCC solid solution with a large volume because the Ti atoms are easily surrounded by Co-rich or Cu-rich or Ni-rich atomic clusters with a relatively large volume and the atomic radii and electronegativity of these three alloying elements are the closest, which also helps to retain the short-range ordered structure in the atomic clusters. The

Table 1: Space group, lattice constant, cell volume, density and relative content of CoCuNiTi and CoCuNiTi + 1 *w*/% CeO₂ alloys

Alloy	Phase	Space group	Lattice constant (nm)	Cell volume (nm³)	Density (g/cm³)	Relative content (*w*/%)
CoCuNiTi	BCC	Im-3m(229)	0.329963	0.03592	4.4278	33.1
	FCC	Fm-3m(225)	0.414638	0.07129	5.9205	66.9
CoCuNiTi +1%CeO₂	BCC	Im-3m(229)	0.333840	0.03721	4.2753	95.7
	FCC	Fm-3m(225)	0.418555	0.07333	5.7558	4.3

close-packed planes of FCC and BCC structures in solids are (111) and (110) respectively, so most (111) crystal planes in the clusters with a large amount of alloying elements with FCC structure are easy to be retained. However, owing to the variety of alloying elements, the large difference in atomic radius, the short residence time at high temperature and the difficulty of cooperative diffusion between elements, it is more difficult for the atoms far away from the central atom to form a periodic and symmetric regular arrangement in the process of nucleation and growth, which makes the diffraction peak intensities of other crystal planes except for close-packed plane lower than the refined calculation values.

The reasons for the increase in BCC phase content for the CoCuNiTi coating with 1 w/% CeO₂ are:

1) CeO₂ can improve the temperature gradient and solidification rate during solidification, and increase the fluidity and wettability of the melt and the diffusion rate of the required alloying elements in the melt, which is helpful to the growth of the Ti-rich BCC primary phase.

2) CeO₂ is easy to ionize and release oxygen at high temperature. As a surface-active element and spherical element, Ce is beneficial to reducing the resistance of Ti nucleation and growth from the melt (such as surface free energy).

3) Ce has the largest positive mixing enthalpy with Ti, and has a lower negative mixing enthalpy with other elements, which reduces the enrichment of Ti in the Ce-rich region in the alloy melt. Since Ti has the highest melting point and Ce has the lowest melting point, the above repulsion will continue for the whole solidification process, thereby reducing the diffusion distance and resistance of the required alloying elements for the growth of the Ti-rich BCC phase.

4) During the solidification process, it is not conducive to the formation of a stable solid solution structure between Ce and other alloying elements under a lower driving force because Ce has the smallest electronegativity and the largest atomic radius. At the same time, the melting point of Ce is much lower than that of the other alloying elements, so it can provide a longer time and lower viscosity liquid environment for the precipitation and growth of other element phases at the same temperature, which is conducive to the diffusion of alloying elements.

5) For CoCuNiTi HEAC with 1 w/% CeO₂, although the relative content of CeO₂ is relatively low, the absolute amount of CeO₂ is relatively large. The above-mentioned repulsion and favorable liquid environment caused by the CeO₂ addition contributes to the increase of nucleation rate and particle size of Ti-rich phase with BCC structure. Co and Ni atoms with a smaller atomic radius are also easy to adhere to the surface of the Ti-rich primary phase and form a stable solid solution owing to the negative maximum mixing enthalpy between Ti and Co/Ni, which is easy to generate Ti-rich BCC main phase.

As described in **Figure 1b**, XRD data of CoCuNiTi HEAC with 1 w/% CeO₂ has little error with the results of the whole pattern fitting and Rietveld refinement, which also indicates that the diffusion of the alloying elements is more sufficient and the atomic arrangement on each diffraction crystal plane is more regular.

Table 2: Characteristic parameters of alloying elements

Element	Melting point (°C)	Electro-negativity	Atomic radius (nm)	Lattice structure
Co	1495	1.88	0.125	FCC/ HCP
Cu	1083	1.90	0.128	FCC
Ni	1453	1.91	0.125	FCC
Ti	1660	1.54	0.146	BCC/HCP
Ce	798	1.12	0.182	FCC

Table3: Atomic radius difference and mixed enthalpy between the various elements[17,18]

	Element	Co	Cu	Ni	Ti	Ce	
Atomic-size difference (%)	Co	-	6	0	-28	-18	Mixed enthalpy (kJ/mol)
	Cu	1.19	-	4	-9	-21	
	Ni	0.00	1.19	-	-35	-28	
	Ti	7.75	6.57	7.75	-	18	
	Ce	18.57	17.42	18.57	10.98	-	

Figure 2 shows the relationship between the diffraction-peak area or full width at half maximum (FWHM) and the diffraction angle for CoCuNiTi coatings before and after adding CeO₂. In order to facilitate the comparison between different samples, the diffraction peak area in **Figure 2** is normalized based on the area of the strongest peak. According to **Table 1** and **Figure 2**, the lattice constants of the BCC main phase and the FCC phase in the alloy coating with 1 w/% CeO₂ are increased and the diffraction peak angles are decreased compared with CoCuNiTi coating. According to the Bragg Equation (3)
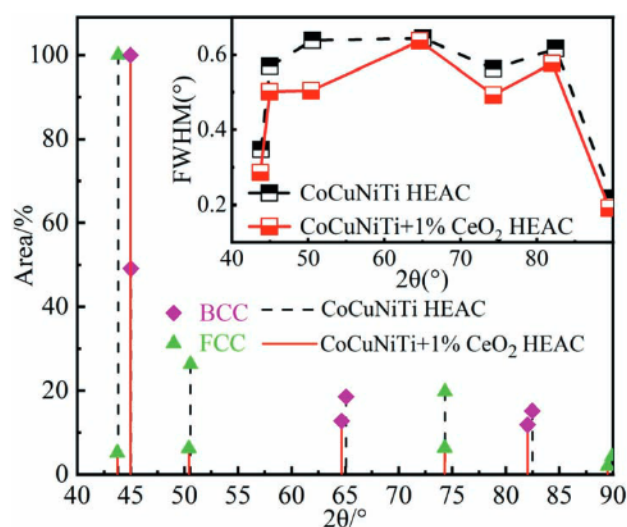

Figure 2: Relationship between diffraction peak area or FWHM and diffraction angle of BCC and FCC phase for CoCuNiTi and CoCuNiTi + 1 w/% CeO₂ HEACs

and the relationship between the crystal plane spacing d and the interference index,

$$2d \sin \theta = \lambda \qquad (3)$$

$$d = \frac{a}{\sqrt{h^2 + k^2 + l^2}} \qquad (4)$$

where θ is the diffraction angle, λ is the wavelength, a is the lattice constant, and h, k and l are the crystal plane index. From **Table 2**, because the atomic radius of Ce is much larger than that of other alloying elements, when Ce atoms enter the lattice sites of other alloy phases, the crystal plane spacing d and lattice constant a will inevitably increase, resulting in the diffraction angle θ shift in a small angle direction. It can be seen from the illustration in **Figure 2** that the FWHM of all the diffraction peaks increases for CoCuNiTi HEAC with 1 $w/\%$ CeO$_2$. This is because Ce produced by CeO$_2$ ionization is a surface-active element and spherical element, which can restrict the grain growth and refine the structure, thus increasing the FWHM of the diffraction peak.

Figure 3 is the metallographic photographs of CoCuNiTi HEACs before and after the addition of 1 $w/\%$ CeO$_2$. It can be seen from **Figure 3** that the microstructures of the two alloy coatings are typical dendrite structures. In the cladding region near the substrate, the dendrite branches are almost perpendicular to the substrate, because most of the heat of the molten cladding layer is lost by heat conduction through the unmelted matrix area

Figure 3: OM photographs of HEACs: a) CoCuNiTi, b) CoCuNiTi + 1 $w/\%$ CeO$_2$

in close contact with its bottom after the laser heat source leaves. Although the orientations of the dendrites in the cladding layer may be different from each other during the initial stage of solidification, the growth rate of dendrites is faster when the dendrite orientation is approximately the same as the opposite direction of heat loss due to the maximum temperature gradient in the direction perpendicular to the substrate. The dendrites with favorable orientation will preferentially extend away from the matrix and inhibit the growth of adjacent dendrites with unfavorable orientation, and gradually form macroscopic columnar dendrites nearly perpendicular to the substrate. The width of the primary dendrites of CoCuNiTi HEACs before and after the addition of 1 $w/\%$ CeO$_2$ is about 8.10 μm and 6.51 μm, respectively. In addition, it can also be seen from **Figure 3** that the width of the columnar dendrite region in the cladding layer with 1 $w/\%$ CeO$_2$ is narrower than that in the sample without CeO$_2$. This is because the composition overcooling can easily occur when other alloying elements with relatively low content are added to the alloy. As the columnar dendrites gradually grow, the solute concentration in front of the solid-liquid interface increases due to solute redistribution, which is easy to generate free dendrites by heterogeneous nucleation owing to the increase in the composition overcooling area at the tip of the columnar dendrite growth direction and block the unidirectional extension of the columnar dendrites. With the full heat exchange between the solidified cladding layer and the substrate, the temperature difference between substrate surface and cladding layer decreases gradually. When the distance between solid-liquid interface and substrate surface increases, the heat dissipation effect is getting closer in the two directions of heat convection or heat radiation towards the top of the cladding layer and heat conduction towards the substrate, which is also beneficial to the formation of free dendrites at the top of the cladding layer.

Figure 4 is SEM images of the CoCuNiTi HEACs before and after adding 1 $w/\%$ CeO$_2$. According to the XRD analysis results in **Figure 1** and **Table 1** and the morphology structure in **Figure 4**, the change of the BCC and FCC phase ratio is consistent with that of the dendrite and interdendrite (ID) region area ratio in the CoCuNiTi HEACs after adding CeO$_2$. Therefore, both HEACs are composed of the dendrite region of BCC phase and the interdendrite region of FCC phase. As shown in **Figure 3** and **Figure 4**, the microstructure of CoCuNITi doped with 1 $w/\%$ CeO$_2$ is obviously refined, mainly because the CeO$_2$ can improve the temperature gradient and solidification rate during solidification, and increase the diffusion rate of the alloying elements required for solid-phase precipitation and growth owing to the improvement of the fluidity and wettability of the melt. Ce is a surface-active element and has the lowest melting point, which helps to reduce the surface free energy that hinders the precipitation of the solid phase and provide a liquid environment with better fluidity, thereby
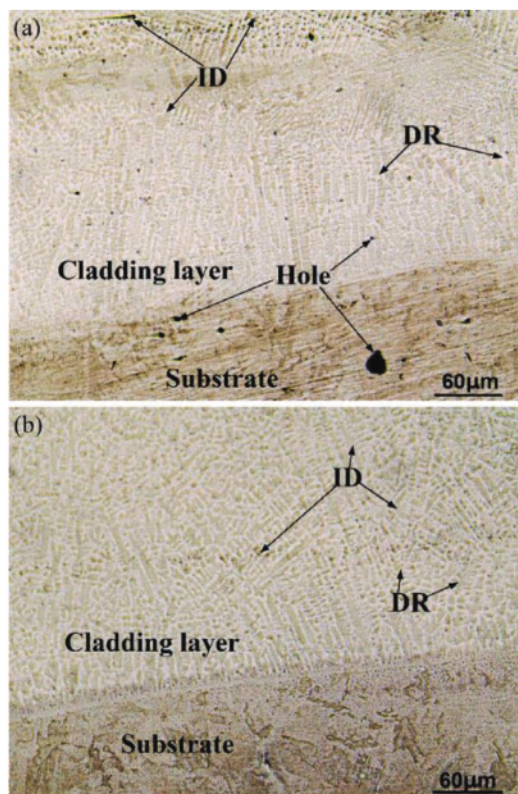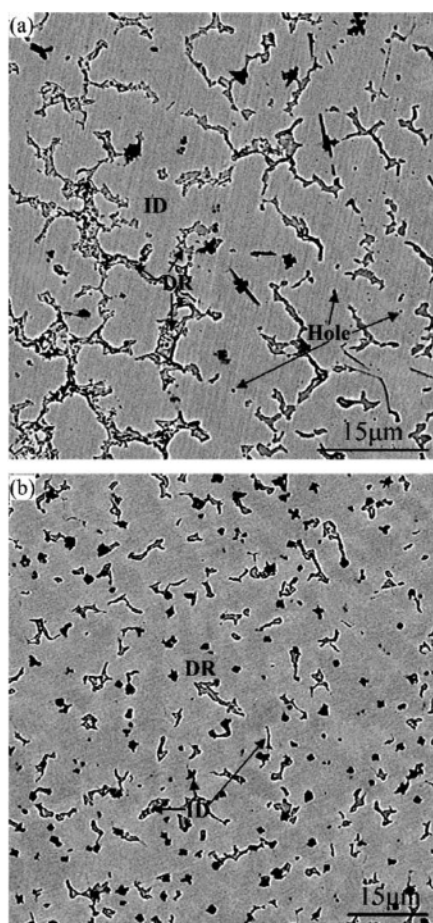
Figure 4: SEM images of CoCuNiTi HEACs: a) without CeO$_2$, b) with 1 w/% CeO$_2$

making the microstructure refined due to the reduction of nucleation and growth resistance. In addition, the hole defects were not significantly observed for CoCuNITi HEAC doped with 1 w/% CeO$_2$ from **Figure 3** and **Figure 4,** mainly because:
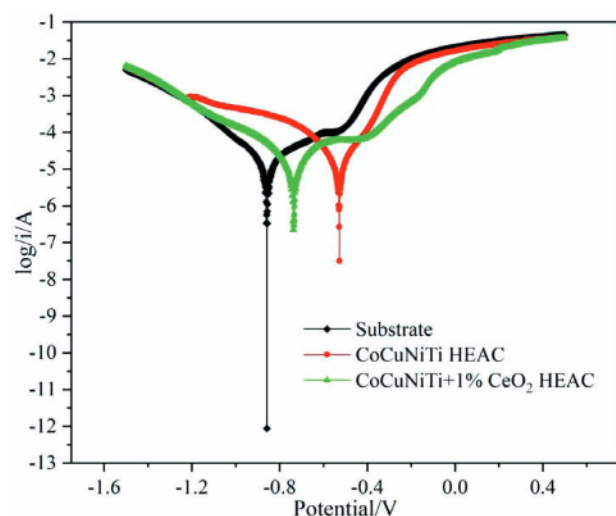

Figure 5: Potentiodynamic anodic polarization curves recorded on the samples in 3.5 w/% NaCl solution

1) The addition of CeO$_2$ can provide a long-time liquid environment and low viscosity, which is conducive to the gas escaping from the melt.

2) The smaller the dendrite spacing is, the finer the microstructure is and the finer the defects are, which reduces the difficulty of gas diffusion escape.

At the same time, the interdendrite region is relatively small, and it is easy for liquid metal to reduce the production probability of hot crack through creep and the living space of the holes during solidification.

Figure 5 shows the potentiodynamic anodic polarization curves of CoCuNiTi HEACs without and with 1 w/% CeO$_2$ and substrate in 3.5 w/% NaCl solution. It can be seen from **Figure 5** that there is no obvious passivation phenomenon in the polarization curves of all the alloys, which is mainly due to the active dissolution behavior because Cl$^-$ has a strong adsorption capacity on the alloy surface and accelerates the corrosion rate. Therefore, when the self-corrosion starts, there is not enough time to form an effective passivation film on the surface of the alloy in a short time, and the alloy has reached the breakdown potential to induce pitting corrosion because Cl$^-$ quickly penetrates the passivation film.[20–22] The corrosion current density (i_{corr}) and corrosion potential (E_{corr}) can be calculated using Tafel line analysis, as shown in **Table 4**. The polarization resistance (R_p) can be calculated using the Stern-Geary Equation (5).[23]

$$i_{corr} = \frac{\beta_a \beta_c}{2.3 R_p (\beta_a + \beta_c)} \quad (5)$$

where β_a and β_c are the slopes of anodic and cathodic curves, respectively. As shown in **Table 4**, the corrosion potential for the two HEACs is larger than that of the substrate, and their corrosion current density and polarization resistance are also smaller than that of the substrate. Based on the electrochemical theory, the corrosion potential can only represent the thermodynamic trend of alloy corrosion, while the corrosion current density is caused by alloy dissolution, and the polarization resistance represents the resistance of this alloy to the corrosion process. According to Faraday's first law of electrolysis and Equation (5), the corrosion rate and the polarization resistance are directly proportional to the corrosion-current density, respectively, and the corrosion resistance of the alloy is closely related to the corrosion current density and polarization resistance. For CoCuNiTi HEAC with 1 w/% CeO$_2$, its corrosion

Table 4: Corrosion characteristics of CoCuNiTi HEACs without and with 1 w/% CeO$_2$ and substrate tested in 3.5 w/% NaCl solution

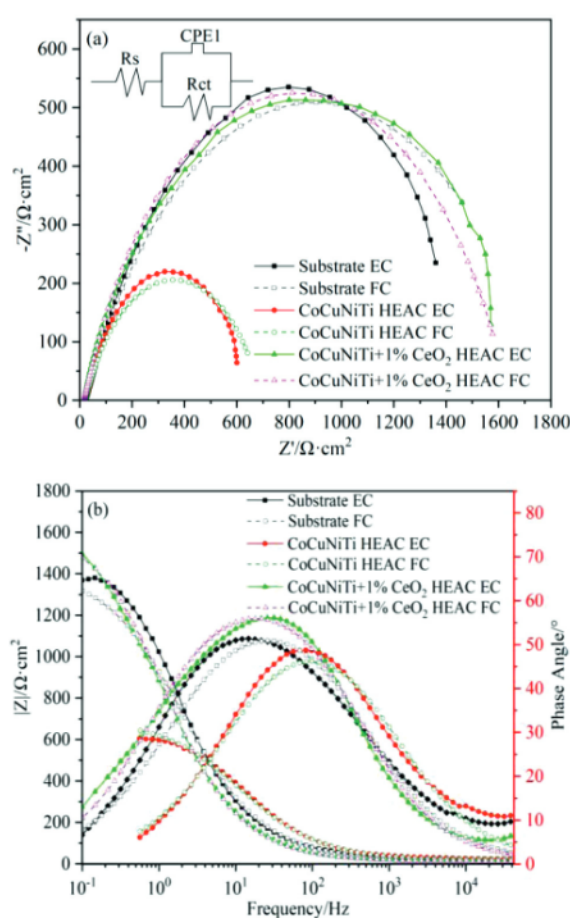| Samples	i_{corr}/ μA·cm^{-2}	E_{corr}/V	β_c/mV	β_a/mV	R_p/ Ω·cm^2
45 steel substrate	12.67	-0.858	182.65	125.38	2551.24
CoCuNiTi	11.78	-0.527	143.10	137.34	2586.57
CoCuNiTi + 1 w/%CeO$_2$	10.59	-0.737	169.46	195.43	3726.26

Figure 6: EIS plots for CoCuNiTi HEACs without and 1 $w/\%$ CeO₂ and 45 steel substrate in 3.5 $w/\%$ NaCl solution: a) Nyquist plots, b) Bode plots

current density (10.59 µA·cm⁻²) is the smallest and its polarization resistance (3726.26 Ω·cm²) is the largest from **Table 4**, so its corrosion resistance is the best.

Figure 6 is the electrochemical impedance spectroscopy (EIS) diagram of without and with 1 $w/\%$ CeO₂ and substrate in 3.5 $w/\%$ NaCl solution. The solid line is the experimental curve (EC), and the dashed line is the fitted curve (FC). The Nyquist diagram shows the hindrance effect between the electrolyte and the sample surface during the electron-transfer process, which is the characteristic of capacitive reactance. The Nyquist curves of all samples show a semi-circular arc characteristic of single capacitive reactance from **Figure 6a** which indicates that the charge transfers between the working electrode surface and the solution, and the electric double-layer capacitance is formed. The electrode reaction is controlled by the interface reaction. The center of the capacitive reactance arc deviates from the real axis, indicating that the electrode surface is not smooth and has a dispersion effect.[24] Generally, the larger the radius of the capacitive arc, the greater the impedance of the sample, and the stronger the corrosion resistance of the metal. The capacitive arc radius of CoCuNiTi HEAC with 1 $w/\%$ CeO₂ is

the largest, so its electrode reaction resistance is the largest, the corrosion rate is the smallest and the corrosion resistance is the best. The Bode diagram in **Figure 6b** shows the relationship between the impedance modulus, the phase angle and the frequency. The Bode diagram provides the information about the charge-transfer resistance, and lg (|Z|) (|Z| is the impedance modulus) at low frequency represents the charge-transfer resistance. As described in **Figure 6b**, the sample with CeO₂ has the largest charge-transfer resistance. The Bode phase angle is related to the time constant. All three alloys have only one capacitance peak, and the changes of their frequency width are proportional to that of their corresponding capacitive reactance arc radius. By comparing the maximum phase angle, it can be seen that the sample with CeO₂ at 56.12° is significantly higher than the other two samples, which also shows that its corrosion rate is relatively lower. Based on the EIS characteristics, the impedance data can be fitted by the equivalent circuit as shown in the illustration in **Figure 6**. The fitting results are shown in **Table 5**, where R_s is the solution resistance, R_{ct} is the charge transfer resistance of the sample in the solution. To better describe the interfacial heterogeneities of the coatings, a constant phase element (CPE) is used, and the impedance Z_{CPE} is calculated (Equation (6)).[24]

$$Z_{CPE} = Y_0^{-1} (j\omega)^{-n} \qquad (6)$$

Where Y_0 is the constant phase element parameter, j is the imaginary number, ω is the angular frequency of the test current, n represents the degree of dispersion effect of the equivalent circuit capacitance, and its calculated value is between –1 and 1. For ideal capacitance circuit, $n = 1$, for porous electrode circuit, $n = 0.7$, for the Warburg diffusion impedance, $n = 0.5$, for ideal resistance circuit, $n = 0$, for ideal inductance circuit, $n = -1$. The smaller the difference between n and 1, the more uniform and denser the electrode surface. The larger the difference between n and 1, the greater the influence of the porous structure on the electrode surface.[24] The n value of CoCuNiTi coating and substrate is approximately equal to 0.7, which is relatively affected by the porous structure. For the sample with CeO₂, n (0.7313) is between 1 and 0.7, indicating that the surface of the cladding layer is relatively dense, which is consistent with the results of the OM and SEM. By fitting the impedance data, it is verified that all the samples have the characteristics of a single capacitive reactance arc and a single time constant, which corresponds to a fitting circuit with a single activation control.[25] R_{ct} represents the electrochemical reaction rate of the electrode/solution interface, and the R_{ct} values of all the samples are much larger than other resistances, which means that the corrosion process of the samples is controlled by the electrochemical reaction at the electrode/solution interface. The R_{ct} value of the CoCuNiTi coating with CeO₂ is about 2.4 times that of the CoCuNiTi coating, indicating that the sample with CeO₂ has a lower corrosion rate in 3.5 $w/\%$ NaCl solution. In addition, the sum of the resistance values of the

sample with CeO$_2$ is significantly larger than that of the other samples, indicating that this sample has the greatest hindrance effect on the current. Therefore, the addition of CeO$_2$ can effectively improve the corrosion resistance of CoCuNiTi coating and substrate. Generally, the corrosion resistance of the alloy coating is closely related to its microstructure. If the chemical composition and microstructure of the alloy coating are not uniform, the differences of the potential and current density on the coating surface are easy to generate and induce corrosion. The CeO$_2$ addition can make the alloy microstructure refine and the defects such as grain boundary and dislocation increase, which can provide the driving force for the growth of the passive film and make the surface generate a dense passive film in the corrosive solution. In addition, CeO$_2$ addition improves the fluidity and solidification characteristics of the alloy, makes the distribution of alloying elements more uniform, and reduces the difference of alloy properties in different areas of the cladding layer, which is easy to prevent Cl$^-$ from penetrating the passivation film and improving the corrosion resistance of the alloy.

Table 5: EIS parameters of CoCuNiTi HEACs without and with 1 w/% CeO$_2$ and substrate in 3.5 w/% NaCl solution 3.5 w/% NaCl

Samples	R_s /$\Omega \cdot cm^2$	CPE1 /$\mu F \cdot cm^{-2}$	n	R_{ct} /$\Omega \cdot cm^2$
45 steel substrate	23.14	159.0	0.6981	1406
CoCuNiTi	22.48	96.79	0.6964	675.3
CoCuNiTi + 1 w/% CeO$_2$	16.84	190.3	0.7313	1622

4 CONCLUSIONS

1) The phase structure of the CoCuNiTi HEAC prepared by laser cladding is a dual-phase structure composed of FCC main phase and BCC phase. The crystal planes corresponding to the diffraction peaks of the two phases are (111), (200), (220), (311) and (110), (200), (211), respectively. The space groups of FCC and BCC belong to Fm-3m (225) and Im-3m (229), respectively. After adding CeO$_2$, the phase structure becomes a dual-phase structure of BCC main phase and FCC phase, and the lattice constants of the two phases increase and the diffraction-peak angles decrease. Space group, lattice constant, cell volume, density and relative content of FCC and BCC were obtained by whole-pattern fitting and Rietveld refinement.

2) The microstructure of the CoCuNiTi HEACs without and with 1 w/% CeO$_2$ is composed of BCC-phase dendrite and FCC-phase interdendrite, which is a typical dendrite structure. The widths of the primary dendrites of the columnar dendrites in CoCuNiTi cladding layer before and after CeO$_2$ doping are about 8.10 μm and 6.51 μm, respectively. No obvious hole defects were found in the CoCuNiTi coating with 1 w/% CeO$_2$.

3) By fitting the impedance data of the two coatings and the substrate, it was verified that all the samples have the characteristics of a single capacitive reactance arc and a single time constant, which corresponds to a fitting circuit with a single activation control. The n value, which represents the degree of dispersion effect of the equivalent circuit capacitance, is the largest for the CoCuNiTi coating doped with CeO$_2$, indicating that the surface of this cladding layer is relatively dense. The CoCuNiTi HEAC with 1 w/% CeO$_2$ has the smallest corrosion current density, the largest capacitive reactance arc radius and polarization resistance, and the best corrosion resistance in 3.5 w/% NaCl solution for these three samples.

5 REFERENCES

[1] W. Li, D. Xie, D. Li, Y. Zhang, P. K. Liaw, Mechanical behavior of high-entropy alloys, Prog. Mater. Sci., 118 (**2021**), 100777, doi:10.1016/j.pmatsci.2021.100777

[2] J. W. Yeh, S. K. Chen, S. J. Lin, J. Y. Gan, T. S. Chin, T. T. Shun, C. H. Tsau, S. Y. Chang, Nanostructured high-entropy alloys with multiple principal elements: Novel alloy design concepts and outcomes, Adv. Eng. Mater., 6 (**2004**) 5, 299–303, doi:10.1002/adem.200300567

[3] C. Zhang, J. Zhu, C. Ji, Y. Guo, R. Fang, S. Mei, S. Liu, Laser powder bed fusion of high-entropy alloy particle-reinforced stainless steel with enhanced strength, ductility, and corrosion resistance, Mater. Design, 209 (**2021**) 11, 109950, doi:10.1016/j.matdes.2021.109950

[4] M. Zhang, E. P. George, J. C. Gibeling, Tensile creep properties of a CrMnFeCoNi high-entropy alloy, Scripta Mater., 194 (**2021**), 113633, doi:10.1016/j.scriptamat.2020.113633

[5] Z. He, N. Jia, H. Yan, Y. Shen, M. Zhu, X. Guan, X. Zhao, S. Jin, G. Sha, Y. Zhu, C. T. Liu, Multi-heterostructure and mechanical properties of N-doped FeMnCoCr high entropy alloy, Int. J. Plasticity, 139 (**2021**), 102965, doi:10.1016/j.ijplas.2021.102965

[6] M. X. Ma, D. C. Zhu, Z. X. Wang, C. Liang, J. C. Zhou, D. L. Zhang, Microstructure and wear resistance of AlCoCrCuFe high-entropy alloy, Adv. Eng. Sci., 50 (**2018**) 4, 208–213, doi:10.15961/j.jsuese.201701019

[7] H. Wan, D. Song, X. Shi, Y. Cai, C. Chen, Corrosion behavior of Al$_{0.4}$CoCu$_{0.6}$NiSi$_{0.2}$Ti$_{0.25}$ high-entropy alloy coating via 3D printing laser cladding in a sulphur environment, J. Mater. Sci. Technol., 60 (**2021**), 197–205, doi:10.1016/j.jmst.2020.07.001

[8] S. Zhang, B. Han, M. Li, Q. Zhang, Y. Wang, Investigation on solid particles erosion resistance of laser cladded CoCrFeNiTi high entropy alloy coating, Intermetallics, 131 (**2021**), 107111, doi:10.1016/j.intermet.2021.107111

[9] Y. B. Peng, W. Zhang, T. C. Li, M. Y. Zhang, Y. Hu, Microstructures and mechanical properties of FeCoCrNi high entropy alloy/WC reinforcing particles composite coatings prepared by laser cladding and plasma cladding, Int. J. Refract. Met. H., 84 (**2019**),105044, doi:10.1016/j.ijrmhm.2019.105044

[10] X. W. Qiu, M. J. Wu, C. G. Liu, Y. P. Zhang, C. X. Huang, Corrosion performance of Al₂CrFeCoₓCuNiTi high-entropy alloy coatings in acid liquids, J. Alloy. Compd., 708 (**2017**), 353–357, doi:10.1016/j.jallcom.2017.03.054

[11] H. Zhang, Y. Pan, Y. Z. He, Synthesis and characterization of FeCoNiCrCu high-entropy alloy coating by laser cladding, Mater. Design, 32 (**2011**) 4, 1910–1915, doi:10.1016/j.matdes.2010.12.001

[12] R. Savinov, Y. Wang, J. Shi, Microstructure and properties of CeO₂ doped CoCrFeMnNi high entropy alloy fabricated by laser metal deposition, J. Manuf. Process., 56 (**2020**), 1245–1251, doi:10.1016/j.jmapro.2020.04.018

[13] M. X. Ma, Z. X. Wang, J. C. Zhou, C. Liang, D. L. Zhang, D.C. Zhu, Effect of CeO₂ doping on phase structure and microstructure of AlCoCuFeMnNi alloy coating, Mater. Res., 22 (**2019**) 1, e20180327, doi:10.1590/1980-5373-mr-2018-0327

[14] Y. S. Tian, C. Z. Chen, L. X. Chen, Q. H. Huo, Effect of RE oxides on the microstructure of the coatings fabricated on titanium alloys by laser alloying technique, Scripta Mater., 54 (**2006**) 5, 847–852, doi:10.1016/j.scriptamat.2005.11.011

[15] M. X. Ma, Z. X. Wang, C. Liang, J. C. Zhou, D. L. Zhang, D. C. Zhu, Effect of CeO₂ doping on microstructure, friction and wear properties of AlCoCrCuFe high-entropy alloys, J. Mater. Eng., 47 (**2019**), 106–111, doi:10.11868/j.issn.1001-4381.2017.001519

[16] M. X. Ma, Z. X. Wang, J. B. Lu, J. C. Zhou, C. Liang, D. C. Zhu, D. L. Zhang, Effect of CeO₂ doping on microstructure and wear resistance of CoCrCuFeMn high-entropy alloy, Trans. Mater. Heat Treat., 40 (**2019**) 9, 50–56, doi:10.13289/j.issn.1009-6264.2019-0137

[17] A. Takeuchi, A. Inoue, Classification of bulk metallic glasses by atomic size difference, heat of mixing and period of constituent elements and its application to characterization of the main alloying element, Mater. Trans., 46 (**2005**) 12, 2817–2829, doi:10.2320/matertrans.46.2817

[18] M. X. Ma, Z. X. Wang, J. C. Zhou, C. Liang, D. L. Zhang, Effect of Ti doping on microstructure and wear resistance of CoCrCuFeMn

[19] M. X. Ma, Z. X. Wang, J. C. Zhou, J. B. Lu, C. Liang, D. L. Zhang, Microstructure and phase transformation of AlCoCrCuFe high entropy alloy, Hot Work. Technol., 47 (**2018**), 31–34, doi:10.14158/j.cnki.1001-3814.2018.14.008

[20] Y. Q. Jiang, J. Li, Y. F. Juan, Z. J. Lu, W. L. Jia, Evolution in microstructure and corrosion behavior of AlCoCrxFeNi high-entropy alloy coatings fabricated by laser cladding, J. Alloy. Compd., 775 (**2019**), 1–14, doi:10.1016/j.jallcom.2018.10.091

[21] N. Kumar, M. Fusco, M. Komarasamy, R. S. Mishra, M. Bourham, K. L. Murty, Understanding effect of 3.5 wt.% NaCl on the corrosion of Al₀.₁CoCrFeNi high-entropy alloy, J. Nucl. Mater., 495 (**2017**), 154–163, doi:10.1016/j.jnucmat.2017.08.015

[22] Y. Wang, M. Y. Li, L. L. Sun, F. Q. Bi, X. Y. Zhang, Microstructure and corrosion property of FeCrNiCo(Cu/Mn)high entropy alloys," Chin. J. Nonferrous Met., 30 (**2020**) 1, 100–108, doi:10.11817/j.ysxb.1004.0609.2020-35715

[23] S. K. Bachani, C. J. Wang, B. S. Lou, L. C. Chang, J. W. Lee, Microstructural characterization, mechanical property and corrosion behavior of VNbMoTaWAl refractory high entropy alloy coatings: Effect of Al content, Surf. Coat. Tech., 403 (**2020**), 126351, doi:10.1016/j.surfcoat.2020.126351

[24] Y. Z. Li, Y. Shi, Microstructure and corrosion resistance of AlCrFeCoNiCu high-entropy coating by laser deposition on an aluminum alloy, Chin. J. Optics, 12 (**2019**) 2, 344–354, doi:10.3788/CO.20191202.0344

[25] Q. Liu, X. Y. Wang, Y. B. Huang, L. Xie, Q. Xu, L. H. Li, Effect of molybdenum content on microstructure and corrosion resistance of CoCrFeNiMo high entropy alloy, Chin. J. Mater. Res., 34 (**2020**) 11, 70–76, doi:10.11901/1005.3093.2020.269